

RESEARCH ARTICLE

10.1002/2017JA024202

Key Points:

- New approach can increase the utility of TEC data and enhance efficiency of analysis of diverse geospace observational system in the future
- For a given season the Southern Hemisphere exhibits correlations over larger distances, but the Northern Hemisphere is more spatially uniform
- Important characteristic ionospheric-scale sizes in TEC data vary across season and hemisphere

Correspondence to:

R. M. McGranaghan,
ryan.mcgranaghan@jpl.nasa.gov

Citation:

McGranaghan, R. M., A. J. Mannucci, O. Verkhoglyadova, and N. Malik (2017), Finding multiscale connectivity in our geospace observational system: Network analysis of total electron content, *J. Geophys. Res. Space Physics*, 122, 7683–7697, doi:10.1002/2017JA024202.

Received 29 MAR 2017

Accepted 3 JUL 2017

Accepted article online 10 JUL 2017

Published online 17 JUL 2017

Finding multiscale connectivity in our geospace observational system: Network analysis of total electron content

Ryan M. McGranaghan^{1,2}, Anthony J. Mannucci², Olga Verkhoglyadova², and Nishant Malik³
¹University Corporation for Atmospheric Research, Boulder, Colorado, USA, ²NASA Jet Propulsion Laboratory, California Institute of Technology, Pasadena, California, USA, ³Department of Mathematics, Dartmouth College, Hanover, New Hampshire, USA

Abstract We present the first complex network theory-based analysis of high-latitude total electron content (TEC) data, including dependencies on interplanetary magnetic field (IMF) clock angle and hemisphere. We examine several network measures to quantify the spatiotemporal correlation patterns in the TEC data for winter and summer months in 2016. We find that significant structure exists in the correlation patterns, distinguishing the dayside and nightside ionosphere, and specific features in the high latitudes such as the polar cap and auroral oval, including the cusp and ionospheric foot points of magnetospheric boundary layers. These features vary with the IMF, exhibiting a strong dependence on the north-south direction and generally larger variations during the winter months in both hemispheres. Our exploratory results suggest that network analysis of TEC data can be used to study characteristic ionospheric spatial scales at high latitudes, thereby extending the utility of these data. We explore mesoscale and large scale (greater than tens of kilometers and greater than hundreds of kilometers, respectively) as a function of winter/summer season, hemisphere, and IMF direction and conclude that the relative importance of different ionospheric scales is not a constant relationship. Together with an identification of important areas of future work, our findings provide a foundation for the application of network analysis techniques to ionospheric TEC. Our results suggest that network analysis can reveal new physical connections in the ionospheric system.

Plain Language Summary Network analysis is a methodology used to investigate the structure and dynamics of a system by identifying objects (nodes) and connections between objects (edges). These methods originated in the social sciences in which people are the objects and connections are defined by the presence of a predefined relationship between people. Network analysis has since flourished and been used to provide new scientific discovery in a broad range of disciplines, including biological, engineering, and geophysical systems. We use this approach to investigate the near-Earth ionized space environment, the ionosphere. Performing a novel network analysis of total electron content (TEC) data, significant structure emerges. Notably, dayside and nightside ionospheric TEC effects are distinct. Further, within the dayside and nightside systems distinct regions emerge in response to space weather activity. We suggest that network analysis can provide significant new, and complementary, understanding of the Earth's space environment and outline important future directions. This work illustrates the importance of data-driven discovery to improve understanding of our space environment and underscores the broader theme of embracing data science in the discipline of heliophysics.

1. Introduction

Global Positioning System (GPS) signals are one of the premier remote sensing tools to facilitate new understanding of space weather phenomena [Coster and Komjathy, 2008]. GPS signal delays due to propagation through the dispersive ionosphere can be used to yield total electron content (TEC) data, which provide critical information about the Earth's ionosphere at higher cadence and over a larger portion of the globe than any other single data source [Mannucci et al., 1998]. Large volumes of data augmented by the proliferation of Global Navigation Satellite Systems around the world and their reliable future availability make these data critical to the future study of the Earth's space environment and its variability, or space weather [Komjathy et al., 2005; Morley et al., 2016].

Global, high-latitude response of TEC is the result of numerous complex geospatial processes, each with unique spatial and temporal scales [Mendillo, 2006; Shim, 2009; Emardson et al., 2013]. Therefore, TEC data are rich with information about the Earth's space environment. Discovery of new information in TEC data may be the key to its use as an auxiliary variable for geospace phenomena. However, the characteristics of TEC data at high latitudes are not well understood, and the complex nature of the processes in this regime requires innovative and sophisticated approaches to (1) understand the information content of these data and (2) gain the most scientific utility from them. In this paper, we attempt to understand the spatiotemporal characteristics of TEC in the high-latitude regime and, therefore, extend the utility of these data.

We present a new approach to the analysis of high-latitude, hemispheric-specific, TEC data known as network analysis. Network analysis [Boccaletti et al., 2006] has been a valuable tool in many fields of research, originating in the social sciences [Milgram, 1967] and finding more recent application in biological, engineering, and geophysical systems [Tsonis et al., 2006; Donges et al., 2009; Steinhäuser et al., 2012; Malik et al., 2012; Dods et al., 2015, 2017]. However, this methodology has never before been applied to TEC data. Networks are defined by nodes, or in geophysical applications, physical grid points, and their connections. We apply network analysis to gridded global TEC data from the months of January and June 2016, where connections are defined by spatiotemporal correlations that exceed a given threshold value. Given the nodes and connections, a network can be constructed and measures calculated to describe the network topology [Newman, 2003]. Network topology can reveal novel understanding of the system it represents [Strogatz, 2001; Albert and Barabási, 2002; Costa et al., 2007]. In this proof of concept paper we examine TEC network topology in the context of space weather phenomena.

This work represents two significant firsts: (1) the first examination of interplanetary magnetic field (IMF) clock angle dependence of high-latitude, hemispheric-specific TEC in magnetic coordinates; and (2) the first application of network methodology to TEC data. Our network analyses suggest that the Southern Hemisphere correlations typically extend over larger distances but that the hemisphere as a whole is more spatially fragmented than the Northern Hemisphere (i.e., the Northern Hemisphere exhibits correlations over shorter distances but is more spatially uniform). The scale sizes important to characterize the ionosphere during geomagnetic activity depend on season and hemisphere. We conclude that our network analyses create a new means for exploring and understanding the geospace system that complements existing approaches, such as empirical orthogonal function analysis [see, e.g., Chen et al., 2015].

The remainder of the paper is laid out as follows. In section 2 we describe the TEC data used. We provide details of our data processing and network analysis in section 3. In section 4 we present and discuss the results and identify important areas of future work. Finally, we conclude the paper in section 5.

2. Data

We process TEC data during January and June 2016 obtained from the Madrigal upper atmospheric science database (<http://madrigal3.haystack.mit.edu/>), which compiles data from the worldwide system of ground-based GPS receivers into 1° latitude \times 1° longitude geographic coordinate distributions at 5 min cadence [Rideout and Coster, 2006; Vierinen et al., 2016]. Madrigal automated processing uses a mapping function to project line-of-sight TEC to the vertical and accounts for various unwanted effects in the signal data, including loss of lock, receiver and transmitter bias, low elevation angles, and outliers. Full details of the processing can be found in Rideout and Coster [2006]. We choose 2016 to take advantage of higher-resolution Madrigal TEC data due to the incorporation of data from additional GPS receivers during that year. On average, ~ 4430 and ~ 5500 stations provide data each day in January and June, respectively. Figure 1 shows the distribution of ground-based GPS receivers on 15 January 2016, which is characteristic for the periods studied in this work. For reference, we superimpose black dotted lines to mark the locations of $\pm 45^\circ$ magnetic latitude (MLAT) in Altitude Adjusted Corrected Geomagnetic Coordinates (AACGM). We present results for MLATs $\geq 48^\circ$ and predominantly discuss behavior at MLATs $\geq 55^\circ$, which is considered high latitude in this work. Station density is greater, and the distribution is more uniform in the Northern Hemisphere. Note that the Madrigal data center provides global maps, and individual station data are not available. We exclude all data for which the Madrigal TEC error estimate exceeds the 95th percentile. Note that we use January instead of December to describe winter conditions in 2016 because December data were not available from the Madrigal website at the time of writing.

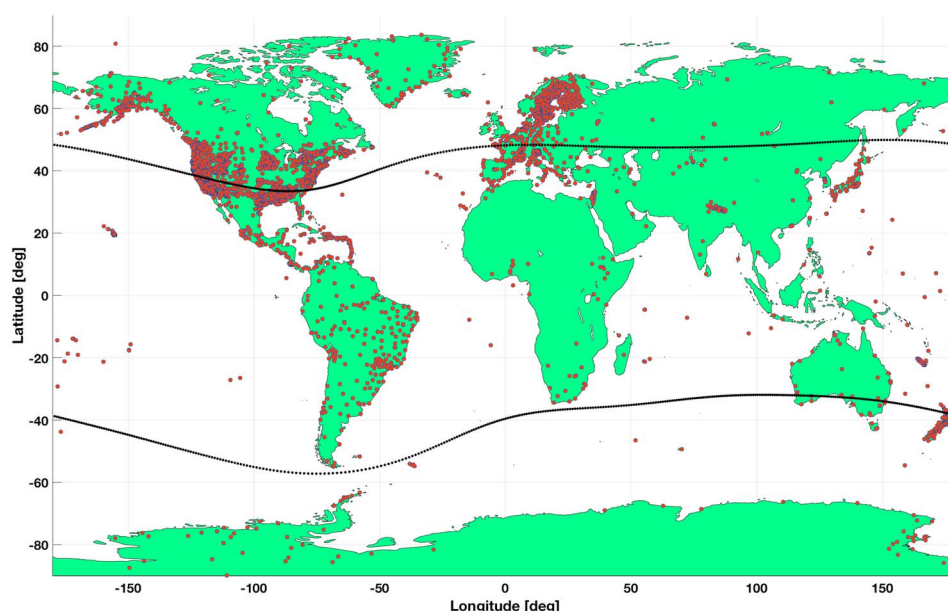


Figure 1. Characteristic geographic distribution of ground-based GPS receivers for the periods studied. Black dotted lines mark the geographic location of $\pm 45^\circ$ magnetic latitudes in Altitude Adjusted Corrected Geomagnetic Coordinates (AACGM), which is the latitudinal range and coordinate system used in this study.

As with any data-driven approach, our exploratory analysis assumes that the properties of the data sufficiently characterize the properties of the observed system. The validity of this assumption is affected by intrinsic limitations in the data, such as resolution and coverage. Though ground-based GPS receiver TEC data provide the best combined spatiotemporal coverage of any single geospace observational system, limitations remain. One such limitation is the uneven distribution of ground-based GPS stations between hemispheres due to ocean coverage. Additionally, because hourly averages of 5 min resolution TEC data are used, we capture the average temporal behavior of phenomena that are manifest on shorter time scales, such as polar and auroral arcs and polar cap patches [Buchau et al., 1983; Jayachandran et al., 2009; Watson et al., 2016a]. We note in our discussion where these limitations may affect physical interpretation. Despite this issue, our analysis provides a distinctly new way to utilize these critical data.

3. Methodology

The Madrigal TEC data are used to form high-latitude networks, using spatiotemporal correlations to determine connections between grid locations. Connected locations then exhibit a shared response to some ionospheric perturbing activity. Our data processing consists of the following steps and is illustrated in Figure 2 (more details will be provided below):

1. The 5 min TEC data are accumulated over 1 h, an hourly median value at each geographic grid point ($1^\circ \times 1^\circ$) is calculated, and these data are converted to AACGM coordinates [Shepherd, 2014]. (Figure 2a shows data already converted to AACGM coordinates.)
2. AACGM data are rebinned onto an equal area grid.
3. Relative perturbation data are computed (equation (1)).
4. Each hourly distribution of relative perturbations is binned by IMF clock angle.
5. A correlation matrix is computed for each clock angle bin.
6. An adjacency matrix is computed from each correlation matrix (equation (3)).
7. The network is constructed, which can be visualized by the network nodes (AACGM grid points) and edges (connections).

We rotate the TEC data into AACGM coordinates because high-latitude ionospheric processes are largely organized by the Earth's magnetic field and are most appropriately analyzed in corrected geomagnetic coordinates [Laundal and Gjerloev, 2014]. We bin the AACGM TEC data into an equal area grid to mitigate the

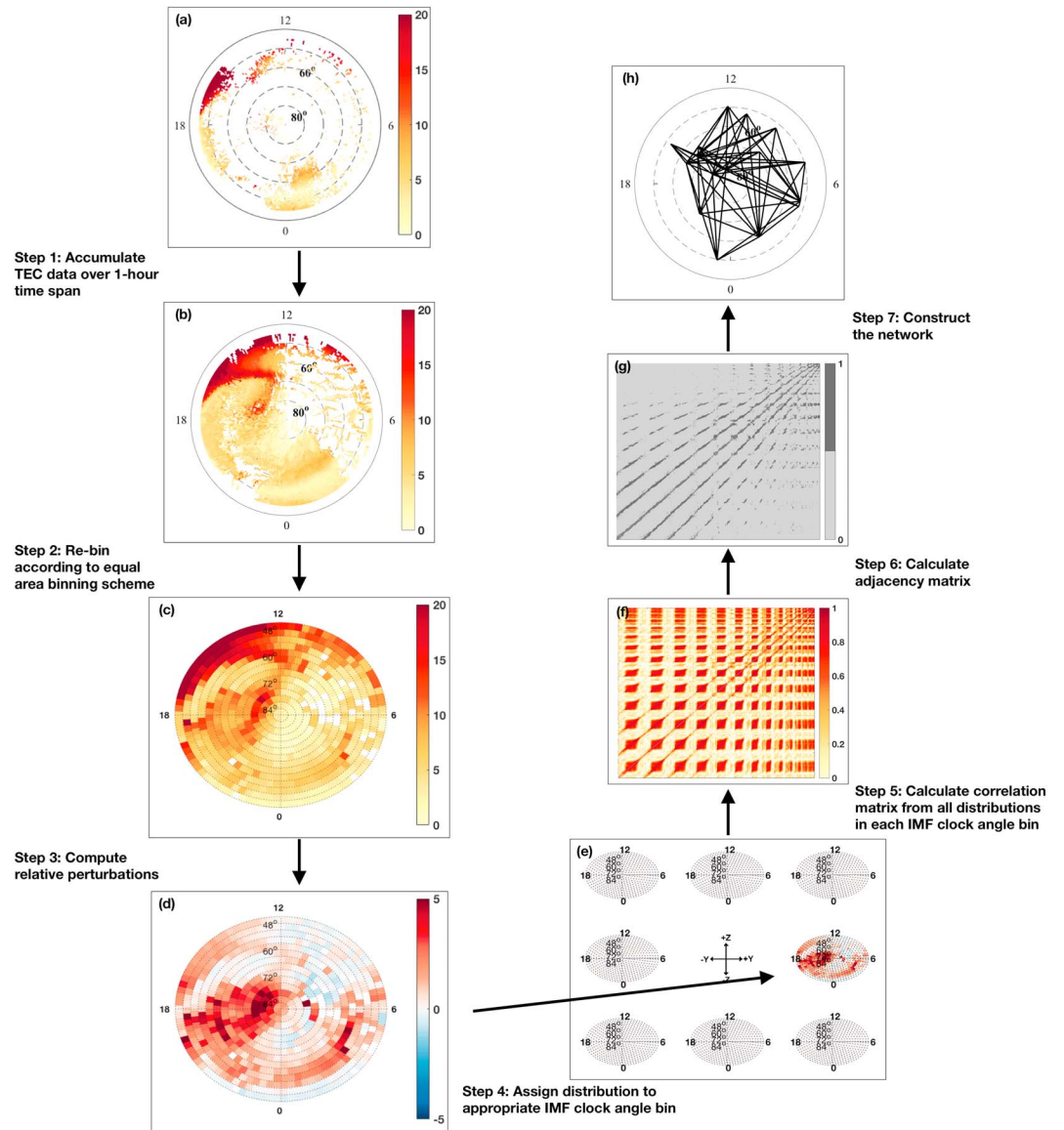


Figure 2. An illustration of the network construction process. (a) Sample 5 min 1° latitude \times 1° longitude total electron content (TEC) distribution from the worldwide system of ground-based receivers used by the Madrigal upper atmospheric science database. These data are shown in magnetic latitude (MLAT)-magnetic local time (MLT) Altitude Adjusted Corrected Geomagnetic Coordinates (AACGM) with noon MLT to the top of the polar plot and a low-latitude limit of 45° . The data plotted are TEC units (TECU), $1 \text{ TECU} = 10^{16} \text{ el/m}^2$. (b) AACGM TEC data accumulated over a 1 h period. (c) TEC data distribution rebinned onto an equal area grid (see text for details). (d) TEC relative perturbation data (equation (1)). All figures in the remainder of the manuscript use the same 45° – 90° MLAT range shown in Figures 2a–2d. (e) Visual showing the assignment of a given relative perturbation distribution to a particular interplanetary magnetic field (IMF) clock angle bin. For all figures in this paper the IMF clock angles increase in 45° increments in the clockwise direction. (f and g) Example correlation and adjacency matrices. (h) Visual illustrating the resultant network where lines have been drawn to indicate that two grid points are connected based on the spatiotemporal correlation between them.

severe latitudinal variation that accompanies a fixed resolution grid in the 45° – 90° latitude range [Ruohoniemi and Baker, 1998]. The equal area gridding scheme uses a constant 3° MLAT resolution and variable magnetic local time (MLT) resolution (0.267 h at 45° MLAT to 4 h at the pole), yielding a total of 672 grid points. Relative perturbations (Step 4 in Figure 2) are calculated from

$$\text{TEC}_{\text{rel. pert}} = \frac{\text{TEC} - \text{TEC}_b}{\text{TEC}_b}, \quad (1)$$

where TEC_b is a background TEC value, chosen to be the monthly median at each grid point for each clock angle bin. A monthly background was chosen to remove long-term variation. We note that defining the most appropriate TEC_b to study geomagnetic activity-driven variations is a difficult problem and that other methods exist [Chen *et al.*, 2017]. However, using the monthly median has a long history of support in the literature [Jakowski *et al.*, 1999; Förster and Jakowski, 2000; Mendillo, 2006, and references therein] and is, therefore, chosen for this work. We found that the network analysis results presented in this paper are relatively insensitive to the choice of TEC_b , likely due to a conservative choice for the threshold used to define connections (see section 3.1). We analyze data from individual months (January and June) separately to remove seasonal variations in our networks. Finally, we accumulate data over 1 h to provide (1) a window of sufficient length to provide global, or nearly global, samples; and (2) data that capture the typical global evolution time scale of geomagnetic disturbances in TEC data. This process results in a time series of relative perturbation data for each grid point equal to the *number of days* \times 24 (744 for January and 720 for June).

We perform separate network analyses on TEC data organized by IMF clock angle, defined as the angle between geocentric solar magnetic (GSM) north and the projection of the IMF vector onto the GSM Y-Z plane:

$$\theta = \tan^{-1} \left(\frac{B_{Y,GSM}}{B_{Z,GSM}} \right), \quad (2)$$

where the GSM coordinate system is centered at the Earth, with x axis oriented toward the Sun, z axis perpendicular to the x axis and in the plane containing the x axis and the Earth's geomagnetic pole (positive northward), and y axis completing the orthogonal set. The y axis is, therefore, positive toward dusk. We define eight IMF clock angle bins, centered at 0° , 45° , 90° , 135° , 180° , 225° , 270° , and 315° and each spanning 45° .

3.1. Complex Network Analysis Applied to High-Latitude TEC Data

The goal of network analysis in the geophysical context is to identify physically meaningful connections among grid points and to determine the physical implications of the resulting network topology. Here we provide further details about steps 5–7 from above (see Figure 2). Given a set of relative perturbation values (for example, relative perturbations for January 2016 when $\theta = 90^\circ \pm 22.5^\circ$), we compute the correlation at zero lag for all possible pairs of nodes and organize the correlations into a matrix. To construct the network out of the correlation matrices, we treat each grid point as a node of the network and correlations between nodes above a given threshold as a connection. Therefore, at its core, network analysis consists of quantifying when pairs of grid point locations are either connected or not, via their zero-lag correlations. The threshold level used to define a connection is a central design consideration in network analysis. In this work we take the threshold to be those correlations in the top 10th percentile, which provides a measure of statistical significance and identifies the most important connections. Analysis not presented here revealed the results to be insensitive to more conservative choices for the threshold level (i.e., higher values of the threshold), indicating that our choice captures the meaningful connections. Each IMF clock angle bin is treated separately such that the threshold level varied across bins. Once this level was determined, TEC networks could be formed and network parameters robustly identified to describe the network topology.

Given the correlation threshold level, we obtain the adjacency matrix, A :

$$A_{ij} = H \left[|c_{ij}| - c_T \right], \quad (3)$$

where c_{ij} is the correlation coefficient between grid point i and grid point j , c_T is the threshold correlation level, and H is the Heaviside step function. From A we compute several robust network measures to investigate the network topology. These measures and their geospatial significance are discussed in detail below and summarized in Table 1.

The first parameter typically examined in network analysis is the degree centrality, which is the simplest measure of the spatiotemporal patterns in the network:

$$C_{D_j} = \frac{\sum_{i=1, i \neq j}^n A_{ij}}{(n-1)}, \quad (4)$$

where C_{D_j} is the degree centrality or the normalized total number of connections, for grid point j , and n is the total number of grid points (672 for the equal area grid). Degree centrality indicates locations that are highly connected [Malik *et al.*, 2012], possibly providing a measure of grid points where critical processes responsible

Table 1. Network Parameters Used to Investigate Network Topology

Network Parameter	Formula	Significance (Interpretation)
Degree centrality (C_{D_j})	Equation (4)	Influence of grid points on network function (larger = greater influence)
Median geodesic separation distance (δ_j)	Equation (5)	Scale sizes of connectivity (larger = longer-range connections)
Local clustering coefficient (C_j)	Equation (7)	Spatial continuity of TEC (larger = more spatially continuous)

for TEC variation take place. We interpret points with greater connectivity to be more indicative of network activity and, therefore, more significant to network function [Costa *et al.*, 2007].

To explore the spatial scales of connectivity, we calculate the median geodesic separation distances for each grid point (δ_j):

$$\delta_j = \text{median} \left(\sum_{i=1, i \neq j}^{k_j} A_{ij} d_{ij} \right), \quad (5)$$

where k_j is the number of connections for grid point j and d_{ij} is the geodesic distance between grid points i and j calculated using the Haversine formula:

$$d_{ij} = R_{\text{iono}} 2 \tan^{-1} \left(\frac{\sqrt{a}}{\sqrt{1-a}} \right), \quad (6)$$

where $a = \sin^2 \left(\frac{\phi_j - \phi_i}{2} \right) + \cos(\phi_i) \cos(\phi_j) \sin^2 \left(\frac{\lambda_j - \lambda_i}{2} \right)$, R_{iono} is the reference ionospheric radius taken to be 6721 km (reference ionospheric altitude of 350 km), ϕ is the latitude, and λ is the longitude. We chose a reference altitude of 350 km to be consistent with previous studies of middle- and high-latitude ionospheric TEC [Spogli *et al.*, 2009; Prikryl *et al.*, 2011], however, because this choice only affects the magnitudes of the geodesic distances and not the relationships it is a relatively inconsequential choice. Note that our metric is the distance on a reference sphere between grid points (i.e., not the graph geodesic) [Newman, 2010]. Assuming that smaller separation distances result in faster information transfer between two points, the median geodesic separation distance could provide insight into how quickly ionospheric TEC adjusts to externally driven disturbances.

Degree centrality provides insight into locations where critical processes contributing to TEC variation occur and the median geodesic separation distance yields information regarding the spatial scales, but neither metric is able to describe the spatial continuity of the variations. We study this using another measure of network topology, the local clustering coefficient. The local clustering coefficient captures the probability that two connected grid points are also connected to the same third grid point:

$$C_j = \frac{2E_j}{k_j(k_j - 1)}, \quad (7)$$

where E_j is the number of connections between the grid points connected to grid point j (note that the total number of possible connections between grid points connected to j is $\frac{k_j(k_j-1)}{2}$, where k_j is as defined above). Therefore, local clustering is a measure of spatial continuity where larger (smaller) values represent clustered (spatially discontinuous) activity [Malik *et al.*, 2012]. Note that the clustering coefficient is independent of the involved spatial scales.

Table 1 summarizes the network parameters.

We used the NetworkX Python language software package to perform the network analyses (<https://networkx.github.io/>).

4. Results and Discussion

4.1. High-Latitude TEC Dependence on IMF Clock Angle

Figure 3 gives occurrence statistics for the IMF clock angle, solar radio flux at 10.7 cm ($F_{10.7}$), disturbance storm time index (Dst), and the planetary Kp index (Kp). Figures 3a and 3e show histograms of the clock angles

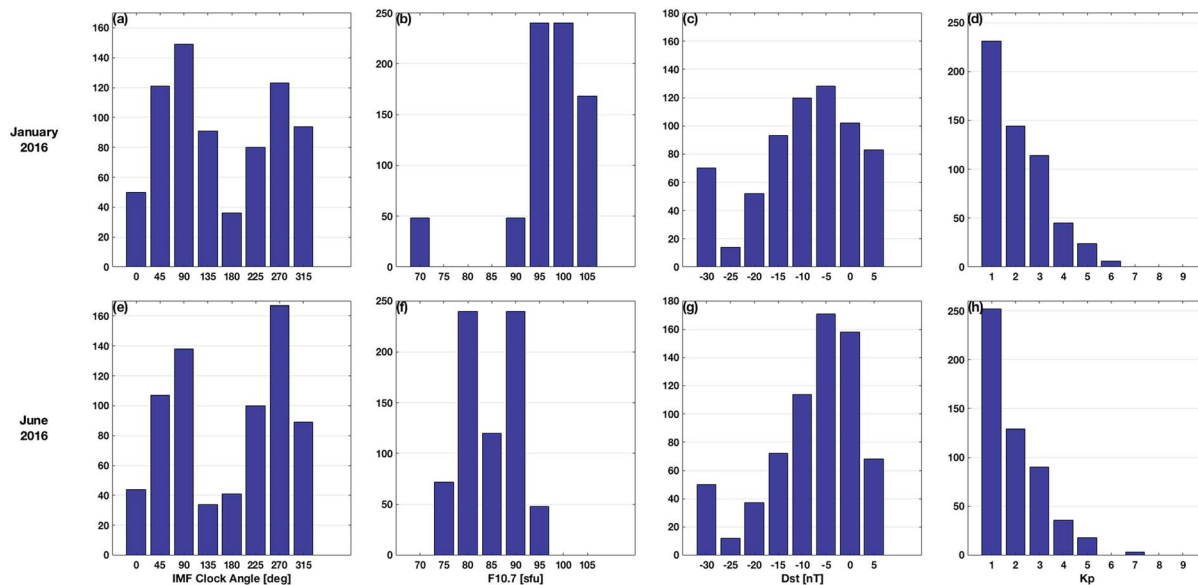


Figure 3. IMF and solar wind occurrence statistics for (a–d) January and (e–h) June 2016. The following data are shown: IMF clock angle (Figures 3a and 3e), $F_{10.7}$ flux (Figures 3b and 3f), Dst (Figures 3c and 3g), and Kp (Figures 3d and 3h). All data have a 1 h temporal resolution.

for January and June 2016, respectively. Solar wind data were obtained from the OMNI database from NASA's Coordinated Data Analysis Web (CDAWeb-<https://cdaweb.sci.gsfc.nasa.gov/>). These data contain measurements from multiple spacecraft, accounting for estimated spacecraft-to-magnetopause propagation times.

Despite fewer occurrences of purely northward and southward IMF (0° and 180° , respectively), which is typical of clock angle occurrence frequencies [Fear *et al.*, 2012], data in the remaining directions were relatively evenly distributed.

Figures 3b and 3f and Figures 3c and 3g provide histograms of $F_{10.7}$ and Dst , respectively. Figures 3b and 3f reveal that $F_{10.7}$ was greater in January ($\overline{F_{10.7}} \sim 100$ solar flux units (10^{-22} Wm $^{-2}$ Hz)) than in June (84.5 solar flux unit). Figures 3c and 3g show similar Dst distributions and indicate common geomagnetic activity during both months ($\overline{Dst}_{\text{January}} = -10.2$ nT, $\overline{Dst}_{\text{June}} = -5.2$ nT) and a relative lack of extreme storms throughout. January contained only 2 h where Dst was below -100 nT, and the June minimum was only -46 nT. The Kp index (Figures 3d and 3h) is a global measure of geomagnetic activity and is shown to provide information on the level of disturbance at middle and high latitudes [Thomsen, 2004] to complement the Dst index, which predominantly measures the level of disturbance at low latitudes. Increasing values of Kp (defined on a scale from 0 to 9) represent increasingly disturbed states of the system. Figures 3d and 3h reveal that the two hemispheres contain very similar behavior at middle and high latitudes ($\overline{Kp}_{\text{January, June}} = 2$).

Figures 4 and 5 show the monthly median background (TEC_b in equation (1)) and relative perturbation distributions for each hemisphere, month, and IMF clock angle, respectively. The Northern Hemisphere distributions are shown in Figures 4a, 4b, 5a, and 5b, the Southern Hemisphere in Figures 4c, 4d, 5c, and 5d, and months are organized by column (winter month in Figures 4a, 4c, 5a, and 5c and summer month in Figures 4b, 4d, 5b, and 5d).

A comparison of the monthly medians during winter (Figures 4a and 4c) and summer months (Figures 4b and 4d) shows the strong influence of solar extra ultraviolet (EUV) radiation on TEC. During winter, the effect of solar influence in the high-latitude regime is reduced given large solar zenith angles. Dayside enhancements in these distributions are limited to relatively low MLATs and in MLT extent. Alternatively, the high-latitude regime during summer is almost completely exposed to direct solar radiation and TEC values are uniformly greater than during winter. Despite the predominance of solar radiation in these distributions, TEC signatures of the statistical, quasi-permanent auroral oval, and its dependence on IMF clock angle are apparent in both winter and summer months. Focusing on the winter hemisphere results given that effects associated with high-latitude geomagnetic activity appear more clearly in TEC with reduced solar irradiation, we see that during southward IMF ($-B_z$, bottom row in Figures 4a and 4c) the auroral oval is located between ~ 60 and

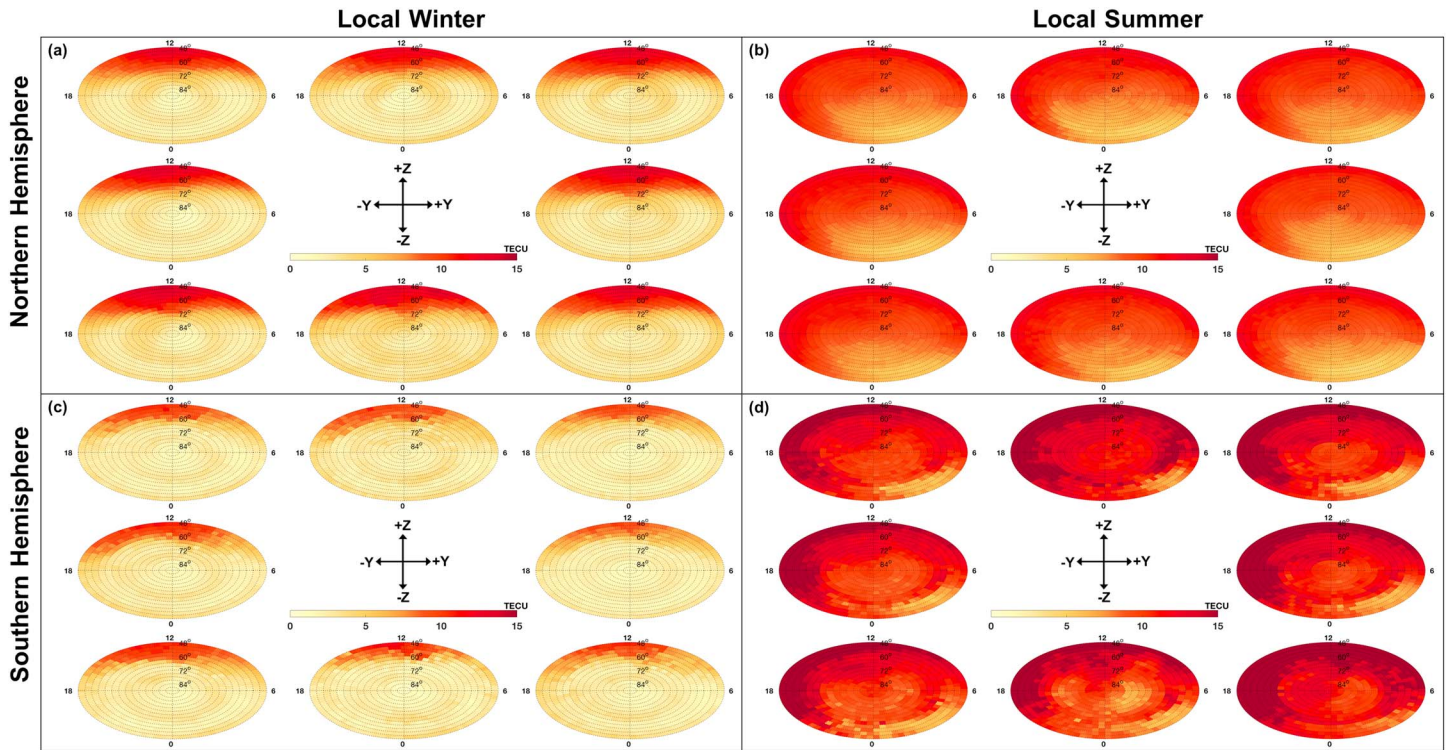


Figure 4. Monthly median TEC distributions, used as TEC_0 in equation (1). Northern and Southern Hemisphere results are shown on the top (panels a and b) and bottom (panels c and d) rows, respectively. The columns are organized by season in the corresponding hemisphere, with local winter to the left (panels a and c) and local summer to the right (panels b and d). The data plotted are TEC units (TECU), $1 \text{ TECU} = 10^{16} \text{ el/m}^2$. Data are shown in MLAT-MLT AACGM coordinates. The low-latitude limit on each polar plot is 45° . The magnetic latitude resolution is 3° , and the magnetic local time resolution is variable to yield equal area bins (0.267 hours at 45° MLAT to 4 hours at the pole). Noon magnetic local time is at the top of each polar plot with dawn to the right. Clock angles increase in 45° increments in the clockwise direction.

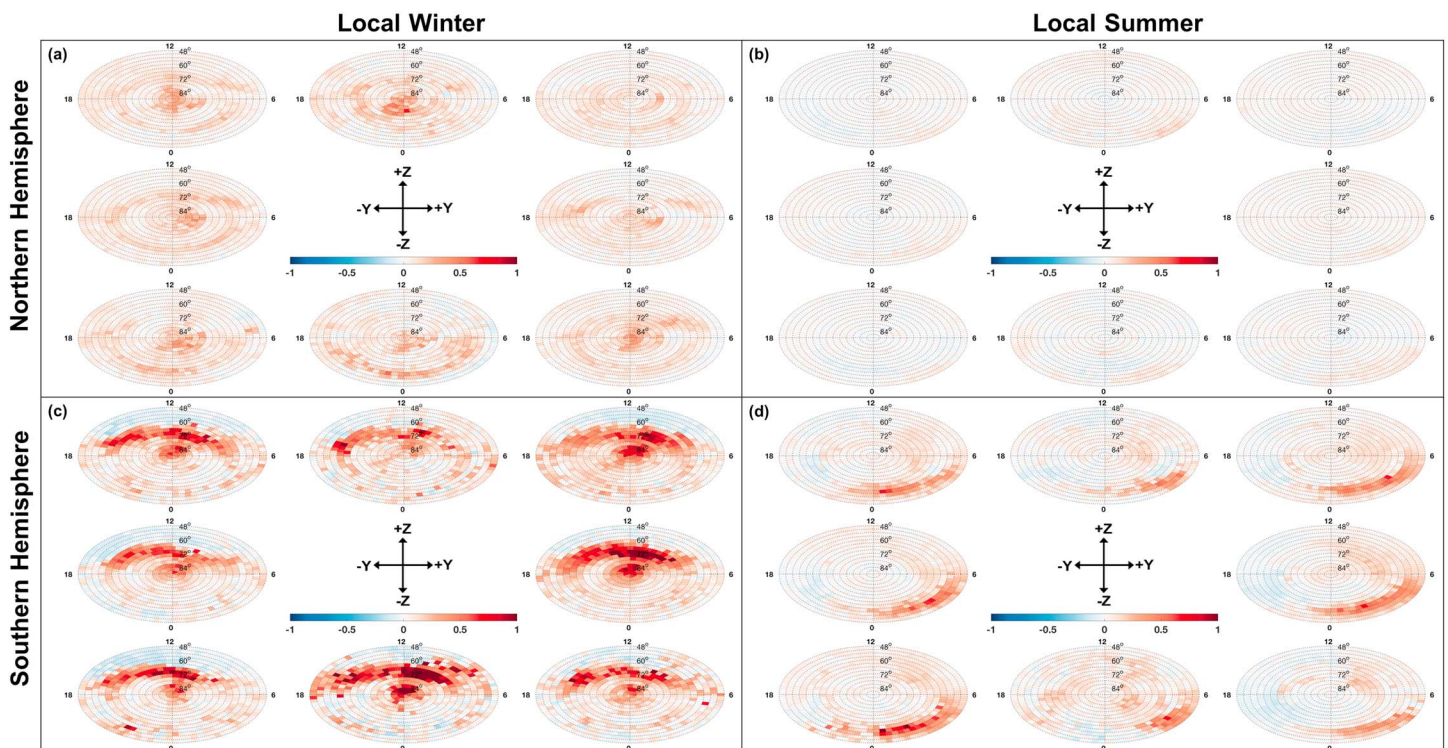


Figure 5. Distributions of average relative perturbations, following the format of Figure 4. A diverging color scheme is used to characterize these data.

70° in a crescent shape extending from premidnight through early morning MLTs to dawn. During northward IMF ($+B_z$, top row in Figures 4a and 4c) the pattern shifts to higher latitudes (almost exclusively $>70^\circ$) and dayside MLTs.

Figure 5 shows the monthly averaged relative perturbations in the same format as Figure 4. Here IMF clock angle dependencies are more distinct. Figure 5a accentuates the $-B_z/+B_z$ differences introduced above, illustrating a shift in TEC enhancement from the nightside auroral oval for $-B_z$ conditions to the dayside high-latitude regime for $+B_z$. This behavior is consistent with high-latitude dynamics due to particle precipitation discussed by McGranaghan *et al.* [2016, and references therein] but not reported before in TEC data. The Southern Hemisphere exhibits larger relative perturbations than the Northern Hemisphere, regardless of season, possibly indicative of increased TEC variability due to a larger offset of the geomagnetic and geographic poles, which causes increased spatial variation of high-latitude activity [see, e.g., Lukianova *et al.*, 2008; Fuller-Rowell *et al.*, 2016, chap. 4 and 5]. The increased variability may also be influenced by observational differences between the hemispheres [Komjathy *et al.*, 1998; Hernández-Pajares *et al.*, 2009]. These differences may also contribute to the fact that the IMF dependence is less clear for the Southern Hemisphere perturbations during local winter (Figure 5c), with large dayside enhancements occurring for $-B_z$ conditions and more subtle changes in the nightside auroral region as the IMF direction changes.

Comparing across rows (Figures 5a versus 5b and 5c versus 5d), it is clear that relative perturbations are smaller during summer. In the Southern Hemisphere during local summer (Figure 5d) an interesting enhancement appears in the postmidnight to dawn MLT sector at MLATs between roughly 45–63°. These enhancements in the relative perturbations correspond to regions of small monthly median TEC values (Figure 4d) and warrant investigation in future work. Finally, during local winter (Figures 5a and 5c) there are relatively large perturbations poleward of $\sim 78^\circ$ MLAT. Such perturbations have been observed previously in statistical analyses of Madrigal data [Clausen *et al.*, 2016] and associated with dayside ionospheric plasma that propagates across the polar cap termed a tongue of ionization (TOI) [Sojka *et al.*, 1994, and references therein]. Figure 5 permits only interpretation of the relative perturbations, and we, therefore, do not make further inferences regarding TOI here. Given the previous findings and the robust quality control process these data have undergone, we believe that these enhancements are physical.

4.2. Spatiotemporal Structuring of High-Latitude TEC: Network Analysis

4.2.1. Degree Centrality

Figure 6 depicts the degree centrality distributions following the format of Figure 4. The degree centrality results are binned in 0.1 increments ($0 < C_{D_i} \leq 0.1$; $0.1 < C_{D_i} \leq 0.2$; $0.2 < C_{D_i} \leq 0.3$; $0.3 < C_{D_i}$) to emphasize distinct spatial regions of degree distribution. Comparing Figures 6a and 6c to Figures 6b and 6d (winter versus summer months), we find that a dayside-nightside distinction emerges as the primary difference between seasons. Therefore, dayside and nightside are the primary regions of network connection, indicating that TEC spatiotemporal variability is coordinated within each regime, but that dayside and nightside responses are distinct from each other. In addition to day/night differences, there are also prominent high-latitude features in the distributions of degree centrality. Figure 6a shows heightened C_{D_i} in the Northern Hemisphere under neutral and $+B_z$ (middle and top rows) at MLATs between ~ 50 and 80° throughout most dayside MLTs, peaking in the ~ 60 – 72° noon MLT sector. These are regions that statistically map to the polar cusp and magnetospheric boundary layers at MLATs $> \sim 70^\circ$ and the central plasma sheet at MLATs between ~ 60 and 70° [Vasyliunas, 1979; Newell *et al.*, 1991; Newell and Meng, 1992]. A future study incorporating magnetospheric information in combination with TEC data using multivariate network analyses will allow further investigation of these potential relationships. Finally, referring to local winter conditions (Figures 6a and 6c) we find that degree centrality in the auroral region is reduced for northward IMF conditions (top row of both Figures 6a and 6c) when compared to southward IMF conditions (bottom row of both Figures 6a and 6c). Roughly defining the auroral region between 57 and 75° MLAT and 20–04 MLT the degree centrality decreases by roughly 30% and 50% between southward and northward IMF in the Northern and Southern Hemispheres, respectively.

The blue values to the bottom left of each polar plot give the global high-latitude degree centrality averages (C_D). Note that values are reduced overall given large areas where C_{D_i} is zero or very small. However, comparison of these average values across summer and winter months reveals that degree centrality is higher in the summer hemisphere than in the winter hemisphere.

Greater degree centrality implies increased importance to the functioning of the network. Therefore, these results suggest that the dayside MLT sector is more important in terms of dynamical processes affecting TEC

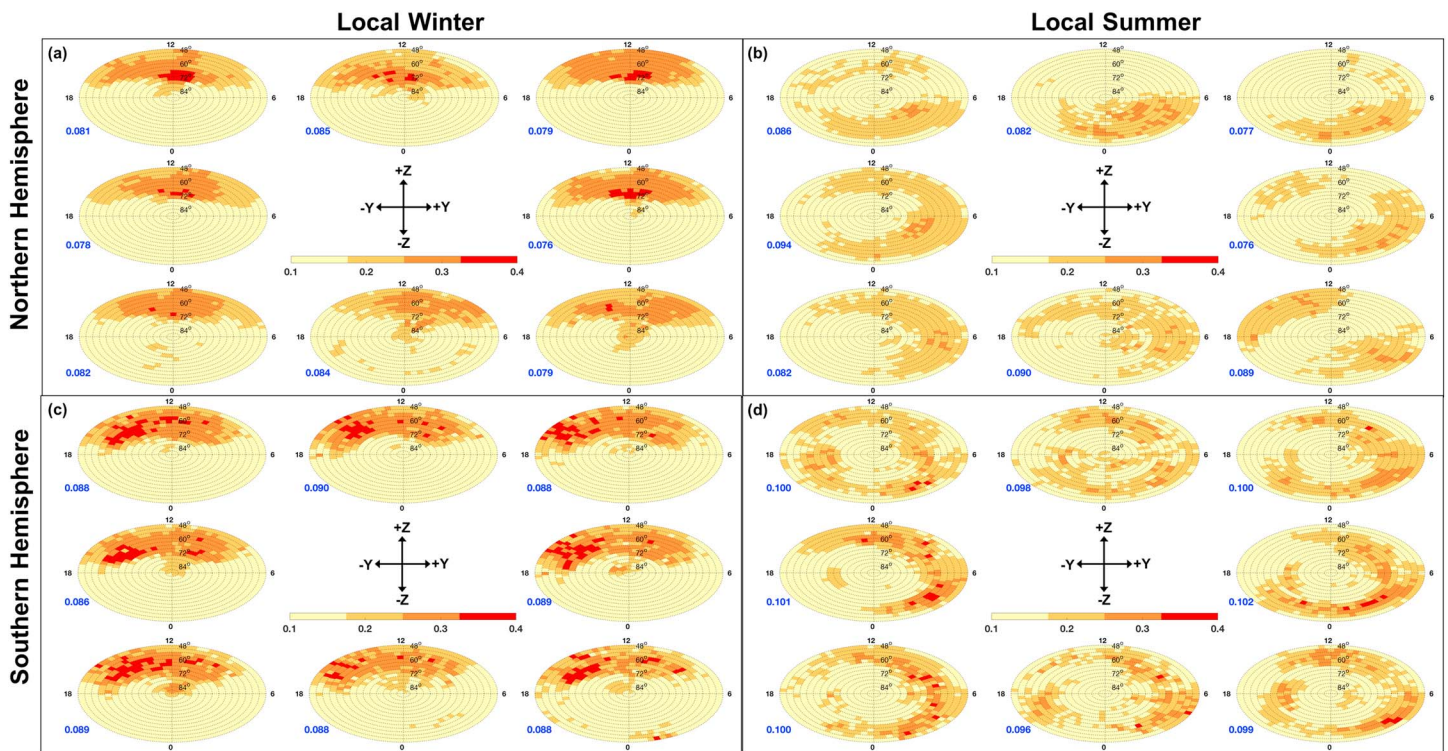


Figure 6. Degree centrality distributions, following the format of Figure 4. The degree centrality results are binned according in 0.1 increments ($0 < C_D \leq 0.1$; $0.1 < C_D \leq 0.2$; $0.2 < C_D \leq 0.3$; $0.3 < C_D$), and global high-latitude averages are shown in blue text to bottom left of each polar plot.

for the winter hemisphere, than for the summer hemisphere, and vice versa. These relationships suggest the potential predictive insight revealed by network analyses.

Large values of degree centrality may emerge due to (1) longer spatial connections or (2) a higher volume of local connections. In order to distinguish these two situations, we next analyze the median length of connections and local clustering coefficient.

4.2.2. Median Geodesic Separation Distance

Figure 7 shows the median geodesic separation distances in kilometers for each grid point. Missing values indicate grid points with zero connections.

Figures 7c and 7d show that the Southern Hemisphere generally has longer-range connections for any given IMF direction, exceeding their Northern Hemisphere counterparts by 500–1500 km on average. The spatial distributions of connection distance in the Northern Hemisphere depends strongly on the IMF direction. Referring to Figure 7a (Northern Hemisphere, winter conditions), a latitudinally expanded auroral region signature is clear during $-B_Z$, while longer connections are recorded in a latitudinally confined auroral region during $+B_Z$. In the $-B_Z$ distribution longer connection distances are also recorded at grid points in the polar cap and at $\sim 60^\circ$ MLAT spanning 1400–1700 MLT. B_Y also contributes to the variability of connection distances. There are interesting longer-range connections at nightside auroral latitudes during $-B_Y$ conditions, becoming less distinct as B_Z rotates from negative to neutral to positive (Figure 7a bottom left, middle, and top, respectively). This is in contrast to the $+B_Y$ distributions, during which connections are largely absent throughout the nightside (i.e., grid points are unconnected and geodesic connection distances are undefined). The Southern Hemisphere during local winter (Figure 7c) shows a reversed B_Y dependence in which $+B_Y$ appears to drive larger connection distances on the nightside than $-B_Y$. Because TEC variability is influenced both by magnetospheric input (e.g., via particle precipitation) and by ionospheric convective transport [Mendillo and Klobuchar, 2006; Thomas et al., 2013], these differences may be a result of convolved magnetospheric and ionospheric effects, which we cannot separate with our results. We provide further discussion of these sources of variability in section 4.2.4. In general, winter hemisphere results are reflected in the summer hemisphere (Figures 7b and 7d) but are less distinct given the heightened overall range of connection.

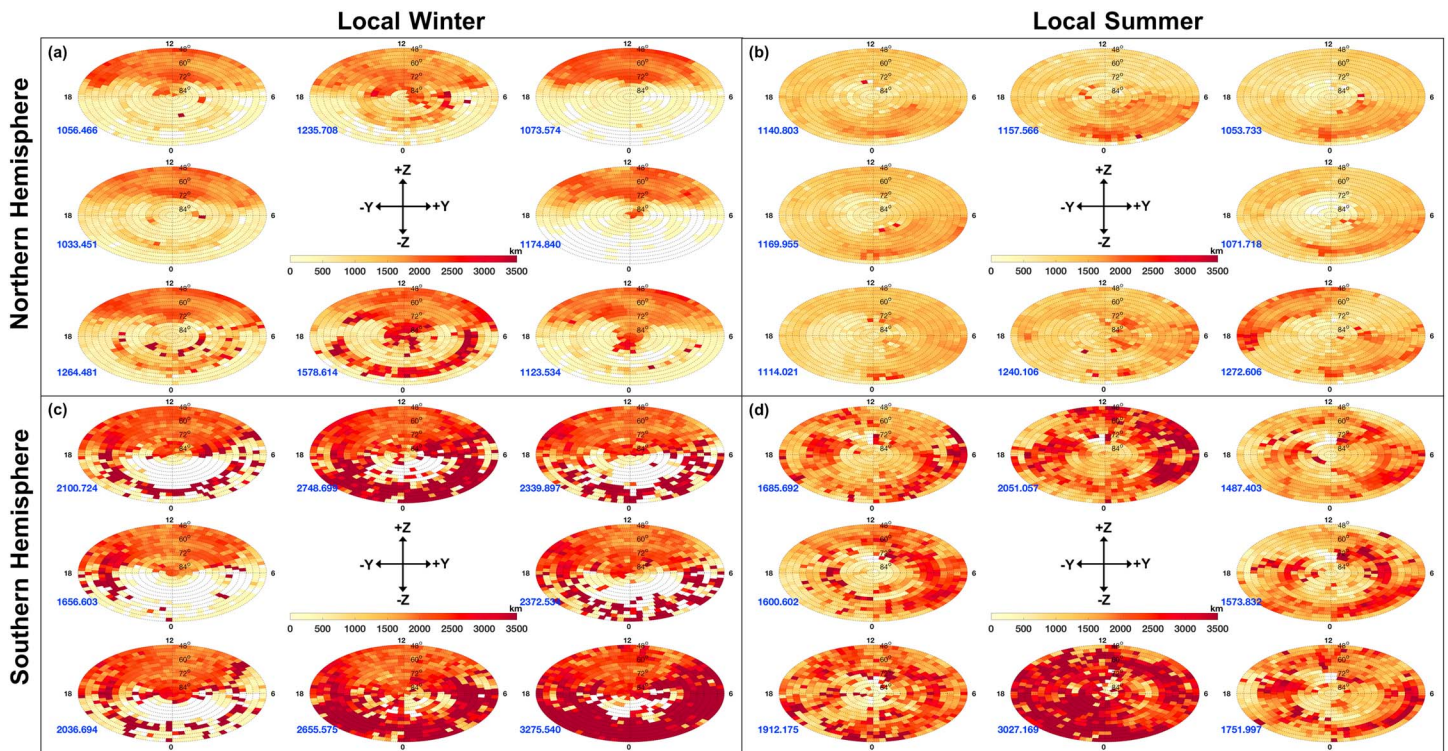


Figure 7. Distributions of median geodesic connection distance (km), following the format of Figure 4. Missing values indicate grid points with zero connections. Global high-latitude averages are shown in blue text to bottom left of each polar plot.

4.2.3. Local Clustering Coefficient

The degree centrality and median geodesic separation distance revealed spatial extent of the TEC networks, but neither provided information about whether the networks are fragmented or spatially continuous. We analyze the clustering coefficient to fill in that gap and associate lower (higher) values with more fragmented (spatially continuous) TEC variability.

Figure 8 shows the local clustering coefficient for each grid point. Like degree centrality, the clustering coefficient results are discretely binned but use 0.2 increments between 0 and 1.

From a comparison of the average values given in blue to the bottom left of each polar plot for the same months in Figure 8 we find that the Northern Hemisphere yields greater global high-latitude averages of the local clustering coefficient than the Southern Hemisphere, despite exhibiting smaller spatial extent of connections (evidenced by smaller values of C_D than the Southern Hemisphere, see Figure 6). This implies that the TEC variability response in the Northern Hemisphere is more spatially continuous but that the Southern Hemisphere has correlations with larger spatial extent. The hemispheric differences may be influenced by different spatial distributions of ground-based GPS receivers in the two hemispheres. This can be addressed by examining subsets of receivers that provide spatially uniform data in both hemispheres. However, Madrigal TEC data do not provide individual station information to perform this analysis, and we leave such an investigation to future work.

Consistent across Figures 6–8 is increased uniformity of connectivity measures in the summer hemisphere (Figures 6b, 6d, 7b, 7d, 8b, and 8d). The winter hemisphere networks, on the other hand, exhibit smaller-scale structuring and an increased dependence on IMF direction. We interpret this to mean that (1) the scale sizes important to characterize the ionosphere exhibit seasonal dependence and (2) geomagnetic activity is either relatively less influential or is suppressed to some extent in the presence of summer conditions [Newell *et al.*, 1996]. The former indicates the importance of performing multiscale analyses of the ionosphere [Moen *et al.*, 2013]. Additional data analysis is required to substantiate these claims. Our network analysis results are summarized in Table 2.

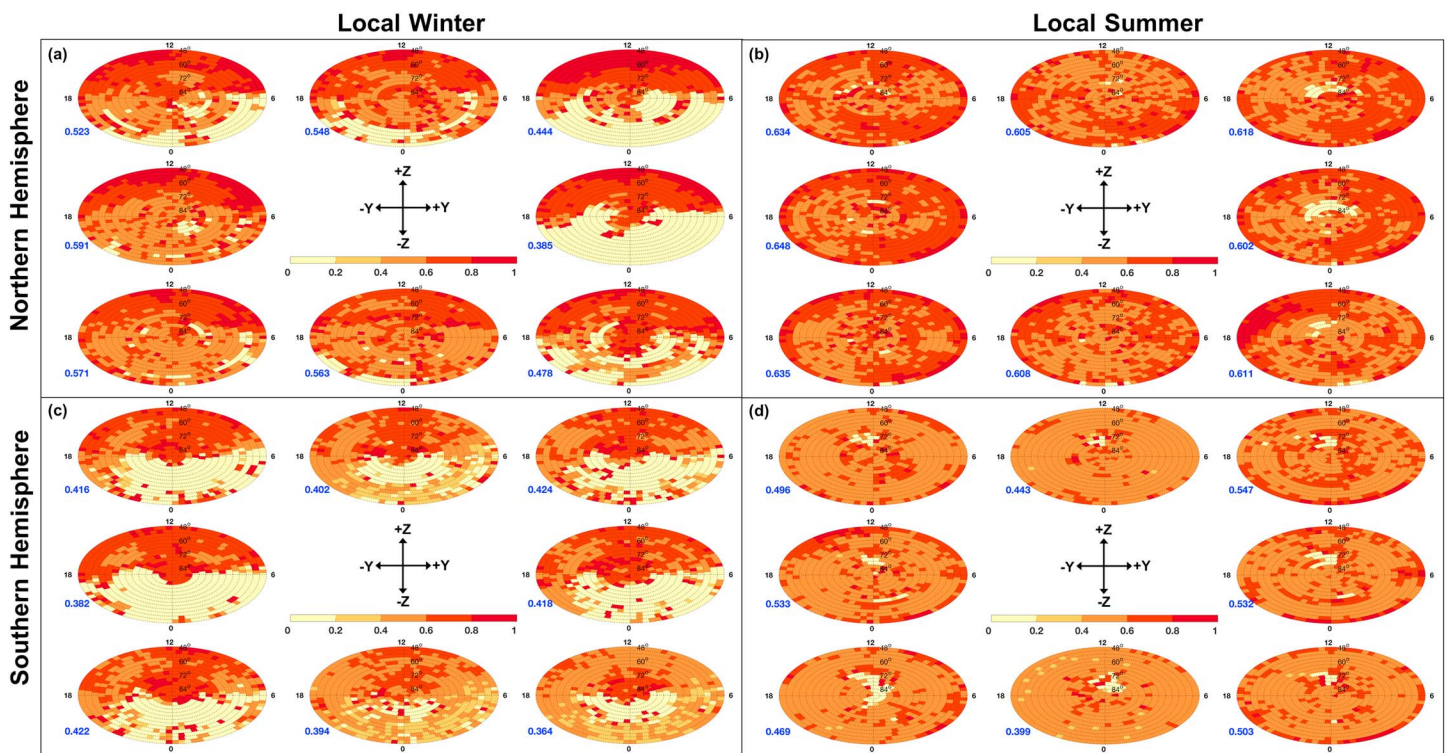


Figure 8. Distributions of local clustering coefficient, following the format of Figure 4. Values are discretely binned between 0.0 and 1.0 with increments of 0.2. Global high-latitude averages are shown in blue text to bottom left of each polar plot.

4.2.4. Mechanisms Controlling the IMF-TEC Relationship

We have commented in this section extensively on IMF dependencies of TEC variability as examined through network analysis. It is useful to provide a brief discussion on the potential physical mechanisms influencing the relationship between IMF and TEC variability. TEC variability at high latitudes is largely controlled by two sources: (1) magnetospheric input (e.g., particle precipitation) and (2) ionospheric plasma transport (e.g., $\mathbf{E} \times \mathbf{B}$ drift). Both sources are heavily dependent on prevailing solar wind conditions, especially the IMF clock angle.

Table 2. TEC Network Analysis Summary Table^a

Result	Significance	Figure(s) of Reference
Dayside and nightside most distinct regions in C_{D_j}	Solar influence extends beyond “background” level of TEC	Figure 6
Lack of spatial continuity in statistical auroral oval during northward IMF (reduced C_{D_j})	No coordinated response in auroral zone to northward IMF	Figure 6
δ_j larger in winter hemisphere on dayside and in the summer hemisphere in regions of known geomagnetic activity variation	Information travels more quickly at dayside MLTs in winter hemisphere and locations of geomagnetic activity in summer hemisphere	Figure 7
Greater values of C_j during southward IMF conditions	Greater spatial continuity during southward IMF	Figure 8
C_j in Northern Hemisphere > C_j in Southern Hemisphere, but C_{D_j} in Southern Hemisphere > C_{D_j} in Northern Hemisphere	Southern Hemisphere has longer-range correlations, but the activity is locally more fragmented	Figures 6 and 8
Summer hemisphere network structure is more uniform	Scale sizes important to ionospheric investigation depend on season and hemisphere, requiring multiscale analyses	Figures 6–8

^aTEC = total electron content, IMF = interplanetary magnetic field, MLT = magnetic local time, C_{D_j} = degree centrality, C_j = local clustering coefficient, and δ_j = median geodesic separation distance.

Magnetospheric particle precipitation exhibits a strong spatial dependence based on IMF clock angle [Korth *et al.*, 2014]. The ionospheric mapping location of these particles determines ionospheric ionization production and, therefore, directly affects TEC. Further, the character of the precipitation changes with IMF conditions, transitioning from predominantly unaccelerated, or diffuse, precipitation during low solar wind driving to accelerated, or discrete, forms as driving increases (i.e., with increasing southward IMF) [Newell *et al.*, 2009, 2010]. Diffuse and discrete precipitation produce drastically different altitudinal ionization profiles and contribute to different TEC behavior and dynamics. The IMF clock angle exerts extensive control over these precipitation characteristics and is a prominent variable in solar wind coupling functions developed to proxy the extent of magnetosphere-ionosphere interactions [Newell *et al.*, 2007; Borovsky, 2013].

Ionospheric plasma transport also contributes to TEC variability. $\mathbf{E} \times \mathbf{B}$ transport depends in large part on the convection electric field imposed on the ionosphere by the magnetosphere. The dependence of this electric field and the resulting ionospheric convection patterns on IMF clock angle are well documented [Heppner and Maynard, 1987; Weimer, 1995; Ruohoniemi and Greenwald, 1996; Cousins and Shepherd, 2010], and TEC dynamics are closely related [Watson *et al.*, 2016b].

The dependence of TEC on solar wind parameters is strong but highly complex. Understanding this dependency offers the possibility to predict TEC based on solar wind input. Network analysis complements the existing body of work and enhances our ability to quantitatively describe the complexities of this critical relationship.

4.2.5. Discussion of Future Directions

We have presented preliminary results that network analyses are a valuable tool to improve understanding of ionospheric behavior. These techniques open new possibilities for ionospheric research, and we identify two key areas of future work: (1) dynamic and (2) multivariate network analyses. These directions are complementary, and we comment briefly on their synergy here to provide a firm foundation for future extension of our analyses.

Given the volume of TEC data available, carefully selected subsets of the data can be used to study particular geophysical conditions using dynamic networks, similar to the work of Dods *et al.* [2015] for auroral substorms. Additionally, multivariate network analysis can be used to identify relationships between TEC variations and indicators of geomagnetic activity, such as field-aligned current and particle precipitation. Such network analyses are critical to the future use of TEC as a proxy for geomagnetic activity. We plan to extend this analysis to additional years of data. A larger volume of data will help to evaluate if TEC network properties are sensitive to less obvious factors, e.g., IMF B_Y and $F_{10.7}$. Additionally, there are solar wind parameters and geomagnetic activity indicators that we have not addressed here that may be strongly related to TEC variability, such as solar wind dynamic pressure and various coupling functions [Newell *et al.*, 2007; Borovsky, 2013]. Investigation of these parameters will be the focus of future work.

We have not commented on the geophysical drivers (beyond the direction of the IMF) of the network topologies because our analyses do not support such conclusions. However, dynamic multivariate network analysis provides a framework for investigating particular geomagnetic phenomena as detailed by Dods *et al.*, 2015 [2015, 2017]. These analyses could reveal observable signatures of these phenomena that exist in TEC data and will be the focus of a future paper.

5. Conclusions

We conducted the first network analysis of high-latitude hemispheric-specific total electron content (TEC) data obtained from Global Positioning System (GPS) signals with interplanetary magnetic field (IMF) clock angle dependency. Our primary conclusions are the following:

1. Dayside and nightside effects most strongly define the networks, with distinct coordinated responses within these regions.
2. Distinct regions emerge within the dayside and nightside systems, including in the polar cap and auroral zone, which react to geophysical processes together. One of the most strongly connected regions, when it exists distinctly, is a relatively large region of enhancement at dayside local times encompassing the polar cusp, central plasma sheet, and the ionospheric foot point of magnetospheric boundary layers.
3. Network activity indicated closer connections between magnetic latitudes poleward of $\sim 70^\circ$ during northward IMF and within the statistical auroral oval during southward IMF.

Our results indicate that network analysis can identify significant patterns in observational data that are consistent with known geophysical phenomena. This approach can, therefore, provide important new information and elucidate physically related phenomena in the high latitudes. We have identified network methodology as a promising tool for the analysis of TEC data and suggest that similar benefit is possible with other sources of geospatial data. We outlined important areas of future work. Particularly, network analyses of TEC data can be extended to investigate specific geophysical conditions, dynamic responses, and multivariate relationships between TEC and other data from our geospace observational system. We have provided preliminary results that complex system analysis can be used to improve understanding of ionospheric variability and space weather.

Acknowledgments

This research was supported by the NASA Living With a Star Jack Eddy Postdoctoral Fellowship Program, administered by the University Corporation for Atmospheric Research and coordinated through the Cooperative Programs for the Advancement of Earth System Science (CPAESS). Portions of this research were carried out at the Jet Propulsion Laboratory, California Institute of Technology, under a contract with the National Aeronautics and Space Administration. We gratefully acknowledge the Massachusetts Institute of Technology (MIT) Atmospheric Sciences Group for providing the TEC data, which are publicly available from <http://madrigal3.haystack.mit.edu/>, and usage support (funded by NSF grants AGS-1242204 and AGS-1025467). The authors would like to specifically acknowledge and thank Chris Watson for his thoughtful and thorough review of this manuscript.

References

- Albert, R., and A.-L. Barabasi (2002), The statistical mechanics of complex networks, *Rev. Modern Phys.*, **74**(47), doi:10.1103/RevModPhys.74.47.
- Boccaletti, S., V. Latora, Y. Moreno, M. Chavez, and D.-U. Hwang (2006), Complex networks: Structure and dynamics, *Phys. Rep.*, **424**(45), 175–308, doi:10.1016/j.physrep.2005.10.009.
- Borovsky, J. E. (2013), Physics-based solar wind driver functions for the magnetosphere: Combining the reconnection-coupled MHD generator with the viscous interaction, *J. Geophys. Res. Space Physics*, **118**, 7119–7150, doi:10.1002/jgra.50557.
- Buchau, J., B. W. Reinisch, E. J. Weber, and J. G. Moore (1983), Structure and dynamics of the winter polar cap *F* region, *Radio Sci.*, **18**(6), 995–1010, doi:10.1029/RS018i006p00995.
- Chen, Z., S.-R. Zhang, A. J. Coster, and G. Fang (2015), EOF analysis and modeling of GPS TEC climatology over North America, *J. Geophys. Res. Space Physics*, **120**, 3118–3129, doi:10.1002/2014JA020837.
- Chen, Z., J.-S. Wang, Y. Deng, and C.-M. Huang (2017), Extraction of the geomagnetic activity effect from TEC data: A comparison between the spectral whitening method and 28-day running median, *J. Geophys. Res. Space Physics*, **122**, 3632–3639, doi:10.1002/2016JA023412.
- Clausen, L. B. N., J. I. Moen, K. Hosokawa, and J. M. Holmes (2016), GPS scintillations in the high latitudes during periods of dayside and nightside reconnection, *J. Geophys. Res. Space Physics*, **121**, 3293–3309, doi:10.1002/2015JA022199.
- Coster, A., and A. Komjathy (2008), Space weather and the Global Positioning System, *Space Weather*, **6**, S06D04, doi:10.1029/2008SW000400.
- Cousins, E. D. P., and S. G. Shepherd (2010), A dynamical model of high-latitude convection derived from SuperDARN plasma drift measurements, *J. Geophys. Res.*, **115**, A12329, doi:10.1029/2010JA016017.
- Costa, L. F., F. A. Rodrigues, G. Travieso, and P. R. V. Boas (2007), Characterization of complex networks: A survey of measurements, *Adv. Phys.*, **56**(1), 167–242, doi:10.1080/00018730601170527.
- Dods, J., S. C. Chapman, and J. W. Gjerloev (2015), Network analysis of geomagnetic substorms using the SuperMAG database of ground-based magnetometer stations, *J. Geophys. Res. Space Physics*, **120**, 7774–7784, doi:10.1002/2015JA021456.
- Dods, J., S. C. Chapman, and J. W. Gjerloev (2017), Characterising the ionospheric current pattern response to southward and northward IMF turnings with dynamical SuperMAG correlation networks, *J. Geophys. Res. Space Physics*, **122**, 1883–1902, doi:10.1002/2016JA023686.
- Donges, J. F., Y. Zou, N. Marwan, and J. Kurths (2009), The backbone of the climate network, *Europhys. Lett.*, **87**(4), 48007.
- Emardson, R., P. Jarlemark, J. Johansson, and S. Schäfer (2013), Spatial variability in the ionosphere measured with GNSS networks, *Radio Sci.*, **48**(5), 646–652, doi:10.1002/2013RS005152.
- Fear, R. C., M. Palmroth, and S. E. Milan (2012), Seasonal and clock angle control of the location of flux transfer event signatures at the magnetopause, *J. Geophys. Res.*, **117**, A04202, doi:10.1029/2011JA017235.
- Förster, M., and N. Jakowski (2000), Geomagnetic storm effects on the topside ionosphere and plasmasphere: A compact tutorial and new results, *Surv. Geophys.*, **21**(1), 47–87, doi:10.1023/A:1006775125220.
- Fuller-Rowell, T., E. Yizengaw, P. Doherty, and S. Basu (2016), *Ionospheric Space Weather: Longitude Dependence and Lower Atmosphere Forcing*, *Geophys. Monogr. Ser.*, AGU, Washington, D. C.
- Heppner, J. P., and N. C. Maynard (1987), Empirical high-latitude electric field models, *J. Geophys. Res.*, **92**(A5), 4467–4489, doi:10.1029/JA092iA05p04467.
- Hernández-Pajares, M., J. M. Juan, J. Sanz, R. Orus, A. Garcia-Rigo, J. Feltens, A. Komjathy, S. C. Schaer, and A. Krankowski (2009), The IGS VTEC maps: A reliable source of ionospheric information since 1998, *J. Geod.*, **83**(3), 263–275, doi:10.1007/s00190-008-0266-1.
- Jakowski, N., S. Schlüter, and E. Sardon (1999), Total electron content of the ionosphere during the geomagnetic storm on 10 January 1997, *J. Atmos. Sol. Terr. Phys.*, **61**(3–4), 299–307, doi:10.1016/S1364-6826(98)00130-8.
- Jayachandran, P. T., K. Hosokawa, J. W. MacDougall, S. Mushini, R. B. Langley, and K. Shiokawa (2009), GPS total electron content variations associated with a polar cap arc, *J. Geophys. Res.*, **114**, A12304, doi:10.1029/2009JA014916.
- Komjathy, A., R. Langley, and D. Bilitza (1998), Ingesting GPS-derived TEC data into the International Reference Ionosphere for single frequency radar altimeter ionospheric delay corrections, *Adv. Space Res.*, **22**(6), 793–801, doi:10.1016/S0273-1177(98)00100-8.
- Komjathy, A., L. Sparks, B. D. Wilson, and A. J. Mannucci (2005), Automated daily processing of more than 1000 ground-based GPS receivers for studying intense ionospheric storms, *Radio Sci.*, **40**, RS6006, doi:10.1029/2005RS003279.
- Korth, H., Y. Zhang, B. J. Anderson, T. Sotirelis, and C. L. Waters (2014), Statistical relationship between large-scale upward field-aligned currents and electron precipitation, *J. Geophys. Res. Space Physics*, **119**, 6715–6731, doi:10.1002/2014JA019961.
- Laundal, K. M., and J. W. Gjerloev (2014), What is the appropriate coordinate system for magnetometer data when analyzing ionospheric currents?, *J. Geophys. Res. Space Physics*, **119**, 8637–8647, doi:10.1002/2014JA020484.
- Lukianova, R., C. Hanuise, and F. Christiansen (2008), Asymmetric distribution of the ionospheric electric potential in the opposite hemispheres as inferred from the SuperDARN observations and FAC-based convection model, *J. Atmos. Sol. Terr. Phys.*, **70**(18), 2324–2335, doi:10.1016/j.jastp.2008.05.015.
- Transport processes in the coupled solar wind-geospace system seen from a high-latitude vantage point, *Greenland Space Science Symposium 2007*.
- Malik, N., B. Bookhagen, N. Marwan, and J. Kurths (2012), Analysis of spatial and temporal extreme monsoonal rainfall over South Asia using complex networks, *Clim. Dyn.*, **39**(3), 971–987, doi:10.1007/s00382-011-1156-4.
- Mannucci, A. J., B. D. Wilson, D. N. Yuan, C. H. Ho, U. J. Lindqvister, and T. F. Runge (1998), A global mapping technique for GPS-derived ionospheric total electron content measurements, *Radio Sci.*, **33**(3), 565–582, doi:10.1029/97RS02707.

- McGranaghan, R., D. J. Knipp, and T. Matsuo (2016), High-latitude ionospheric conductivity variability in three dimensions, *Geophys. Res. Lett.*, **43**, 7867–7877, doi:10.1002/2016GL070253.
- Mendillo, M. (2006), Storms in the ionosphere: Patterns and processes for total electron content, *Rev. Geophys.*, **44**, RG4001, doi:10.1029/2005RG000193.
- Mendillo, M., and D. J. A. Klobuchar (2006), Total electron content: Synthesis of past storm studies and needed future work, *Radio Sci.*, **41**(5), RS5S02, doi:10.1029/2005RS003394.
- Milgram, S. (1967), The small-world problem, *Psychol. Today*, **1**(1), 60–67, doi:10.1037/e400002009-005.
- Moen, J., K. Oksavik, L. Alfonsi, Y. Daabakk, V. Romano, and L. Spogli (2013), Space weather challenges of the polar cap ionosphere, *J. Space Weather Space Clim.*, **3**, A02, doi:10.1051/swsc/2013025.
- Morley, S. K., J. P. Sullivan, M. G. Henderson, J. B. Blake, and D. N. Baker (2016), The Global Positioning System constellation as a space weather monitor: Comparison of electron measurements with Van Allen Probes data, *Space Weather*, **14**, 76–92, doi:10.1002/2015SW001339.
- Newell, P. T., and C.-I. Meng (1992), Mapping the dayside ionosphere to the magnetosphere according to particle precipitation characteristics, *Geophys. Res. Lett.*, **19**(6), 609–612, doi:10.1029/92GL00404.
- Newell, P. T., W. J. Burke, E. R. Sánchez, C.-I. Meng, M. E. Greenspan, and C. R. Clauer (1991), The low-latitude boundary layer and the boundary plasma sheet at low altitude: Prenoon precipitation regions and convection reversal boundaries, *J. Geophys. Res.*, **96**(A12), 21,013–21,023, doi:10.1029/91JA01818.
- Newell, P. T., C.-I. Meng, and K. M. Lyons (1996), Suppression of discrete aurorae by sunlight, *Nature*, **381**(6585), 766–767, doi:10.1038/381766a0.
- Newell, P. T., T. Sotirelis, K. Liou, C.-I. Meng, and F. J. Rich (2007), A nearly universal solar wind-magnetosphere coupling function inferred from 10 magnetospheric state variables, *J. Geophys. Res.*, **112**, A01206, doi:10.1029/2006JA012015.
- Newell, P. T., T. Sotirelis, and S. Wing (2009), Diffuse, monoenergetic, and broadband aurora: The global precipitation budget, *J. Geophys. Res.*, **114**, A09207, doi:10.1029/2009JA014326.
- Newell, P. T., T. Sotirelis, and S. Wing (2010), Seasonal variations in diffuse, monoenergetic, and broadband aurora, *J. Geophys. Res.*, **115**, A03216, doi:10.1029/2009JA014805.
- Newman, M. (2010), *Networks: An Introduction*, Oxford Univ. Press, New York.
- Newman, M. E. J. (2003), The structure and function of complex networks, *SIAM Rev.*, **45**(2), 167–256, doi:10.1137/S003614450342480.
- Prikryl, P., P. T. Jayachandran, S. C. Mushini, and R. Chadwick (2011), Climatology of GPS phase scintillation and HF radar backscatter for the high-latitude ionosphere under solar minimum conditions, *Ann. Geophys.*, **29**(2), 377–392, doi:10.5194/angeo-29-377-2011.
- Rideout, W., and A. Coster (2006), Automated GPS processing for global total electron content data, *GPS Solut.*, **10**(3), 219–228, doi:10.1007/s10291-006-0029-5.
- Ruohoniemi, J. M., and K. B. Baker (1998), Large-scale imaging of high-latitude convection with Super Dual Auroral Radar Network HF radar observations, *J. Geophys. Res.*, **103**(A9), 20,797–20,811, doi:10.1029/98JA01288.
- Ruohoniemi, J. M., and R. A. Greenwald (1996), Statistical patterns of high-latitude convection obtained from Goose Bay HF radar observations, *J. Geophys. Res.*, **101**(A10), 21,743–21,763, doi:10.1029/96JA01584.
- Shepherd, S. G. (2014), Altitude-adjusted corrected geomagnetic coordinates: Definition and functional approximations, *J. Geophys. Res. Space Physics*, **119**, 7501–7521, doi:10.1002/2014JA020264.
- Shim, J. S. (2009), Analysis of Total Electron Content (TEC) Variations in the Low- and Middle-Latitude Ionosphere, dissertation, Utah State Univ., Logan, Utah.
- Sojka, J. J., M. D. Bowline, and R. W. Schunk (1994), Patches in the polar ionosphere: UT and seasonal dependence, *J. Geophys. Res.*, **99**(A8), 14,959–14,970, doi:10.1029/93JA03327.
- Spogli, L., L. Alfonsi, G. De Franceschi, V. Romano, M. H. O. Aquino, and A. Dodson (2009), Climatology of GPS ionospheric scintillations over high and mid-latitude European regions, *Ann. Geophys.*, **27**(9), 3429–3437, doi:10.5194/angeo-27-3429-2009.
- Steinhaeuser, K., A. R. Ganguly, and N. V. Chawla (2012), Multivariate and multiscale dependence in the global climate system revealed through complex networks, *Clim. Dyn.*, **39**(3), 889–895, doi:10.1007/s00382-011-1135-9.
- Strogatz, S. H. (2001), Exploring complex networks, *Nature*, **410**(6825), 268–276, doi:10.1038/35065725.
- Thomas, E. G., J. B. H. Baker, J. M. Ruohoniemi, L. B. N. Clausen, A. J. Coster, J. C. Foster, and P. J. Erickson (2013), Direct observations of the role of convection electric field in the formation of a polar tongue of ionization from storm enhanced density, *J. Geophys. Res. Space Physics*, **118**, 1180–1189, doi:10.1002/jgra.50116.
- Thomsen, M. F. (2004), Why *Kp* is such a good measure of magnetospheric convection, *Space Weather*, **2**, S11004, doi:10.1029/2004SW000089.
- Tsonis, A. A., K. L. Swanson, and P. J. Roebber (2006), What do networks have to do with climate?, *Bull. Am. Meteorol. Soc.*, **87**(5), 585–595, doi:10.1175/BAMS-87-5-585.
- Vasyliunas, V. M. (1979), Interaction between the magnetospheric boundary layers and the ionosphere, in *Proceedings of the Magnetospheric Boundary Layers Conference*, vol. 148, edited by B. Battrock et al., pp. 387–393, ESA Spec. Publ., Noordwijk, Netherlands.
- Vierinen, J., A. J. Coster, W. C. Rideout, P. J. Erickson, and J. Norberg (2016), Statistical framework for estimating GNSS bias, *Atmos. Meas. Tech.*, **9**(3), 1303–1312, doi:10.5194/amt-9-1303-2016.
- Watson, C., P. T. Jayachandran, and J. W. MacDougall (2016a), Characteristics of GPS TEC variations in the polar cap ionosphere, *J. Geophys. Res. Space Physics*, **121**, 4748–4768, doi:10.1002/2015JA022275.
- Watson, C., P. T. Jayachandran, and J. W. MacDougall (2016b), GPS tec variations in the polar cap ionosphere: Solar wind and IMF dependence, *J. Geophys. Res. Space Physics*, **121**, 9030–9050, doi:10.1002/2016JA022937.
- Weimer, D. R. (1995), Models of high-latitude electric potentials derived with a least error fit of spherical harmonic coefficients, *J. Geophys. Res.*, **100**(A10), 19,595–19,607, doi:10.1029/95JA01755.